

# **Supporting Information: Bulk-like intrinsic phonon thermal conductivity of micrometer thick AlN films**

Yee Rui Koh<sup>1</sup>, Zhe Cheng<sup>2</sup>, Abdullah Mamun<sup>3</sup>, Md Shafkat Bin Hoque<sup>1</sup>, Zeyu Liu<sup>4</sup>, Tingyu Bai<sup>5</sup>, Kamal Hussain<sup>3</sup>, Michael E. Liao<sup>5</sup>, Ruiyang Li<sup>4</sup>, John T. Gaskins<sup>1</sup>, Ashutosh Giri<sup>1</sup>, John Tomko<sup>6</sup>, Jeffrey L. Braun<sup>1</sup>, Mikhail Gaevski<sup>3</sup>, Eungkyu Lee<sup>4</sup>, Luke Yates<sup>2</sup>, Mark S. Goorsky<sup>5</sup>, Tengfei Luo<sup>4</sup>, Asif Khan<sup>3</sup>, Samuel Graham<sup>2,7</sup>, and Patrick E. Hopkins<sup>1,6,8\*</sup>

<sup>1</sup>*Department of Mechanical and Aerospace Engineering, University of Virginia, Charlottesville, Virginia 22904, USA*

<sup>2</sup>*George W. Woodruff School of Mechanical Engineering, Georgia Institute of Technology, Atlanta, Georgia 30332, USA*

<sup>3</sup>*Department of Electrical Engineering, University of South Carolina, Columbia, South Carolina 29208, USA*

<sup>4</sup>*Department of Aerospace and Mechanical Engineering, University of Notre Dame, Notre Dame, Indiana 46556, USA*

<sup>5</sup>*Department of Materials Science and Engineering, University of California at Los Angeles, Los Angeles, California 90095, USA*

<sup>6</sup>*Department of Materials Science and Engineering, University of Virginia, Charlottesville, Virginia 22904, USA*

<sup>7</sup>*School of Materials Science and Engineering, Georgia Institute of Technology, Atlanta, Georgia 30332, USA*

<sup>8</sup>*Department of Physics, University of Virginia, Charlottesville, Virginia 22904, USA*

\*Corresponding author: [peh4v@virginia.edu](mailto:peh4v@virginia.edu)

## **1. Boltzmann Transport Equation (BTE) of the AlN Thermal Conductivity**

Figure S1 below examines the accumulative AlN thermal conductivity dependence on the phonon mean free path from 100-500 K. Both in-plane and cross-plane thermal conductivity values of the AlN are included in the figure. The sub-micron mean-free-path (MFP) contribute only partially to the AlN bulk thermal conductivity, defined as an intrinsic effect in Ref. [S1]. Previous literature [S1, S2, S3] either varied AlN film thicknesses or modulated pump frequency to study the intrinsic effects. However, the thermal transport of these studies might be affected by the extrinsic effects from the interfaces, i.e., Al/AlN and AlN/Al<sub>2</sub>O<sub>3</sub> of the samples. The interpretation of these findings might be complicated due to mixing of both intrinsic and extrinsic effects on thermal transport.

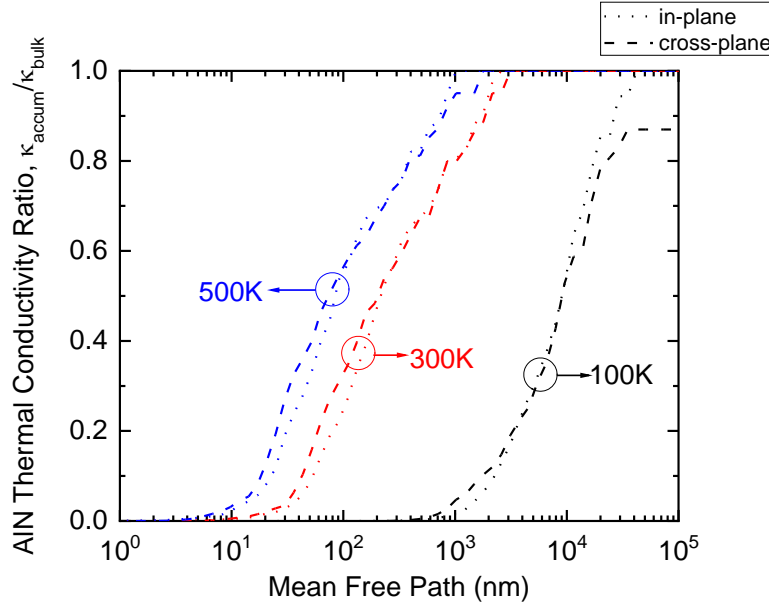


Figure S1 The AlN thermal conductivity ratio,  $\kappa_{accum}/\kappa_{bulk}$  versus the phonons mean-free-path, for in- and cross-plane direction.

The BTE bulk thermal conductivity of the AlN for in- and cross-plane for 100, 300, and 500 K are shown in Table S1 below. Our measurements show a good agreement with the calculated bulk thermal conductivity at 300 K and 500 K, but significantly lower compared to the calculated bulk thermal conductivity at 100 K. We believe this observation is due to the limited film thickness and the interface scattering mechanism at the AlN/Al<sub>2</sub>O<sub>3</sub>. Due to the reciprocal space grid size limitation and the long mean free paths at low temperature, BTE prediction at lower temperature can also have higher uncertainties.

Table S1: In-plane and cross-plane AlN bulk thermal conductivity from 100-500K.

Temperature (K)	In-plane bulk thermal conductivity (W m <sup>-1</sup> K <sup>-1</sup> )	Cross-plane bulk thermal conductivity (W m <sup>-1</sup> K <sup>-1</sup> )
100	3381.7	3383.3
300	299.0	282.2
500	148.8	140.3

The calculated phonons lifetime and MFP in the function of phonon frequency, and calculated phonon dispersion of AlN via BTE model are shown in Figure S2 and S3 respectively.

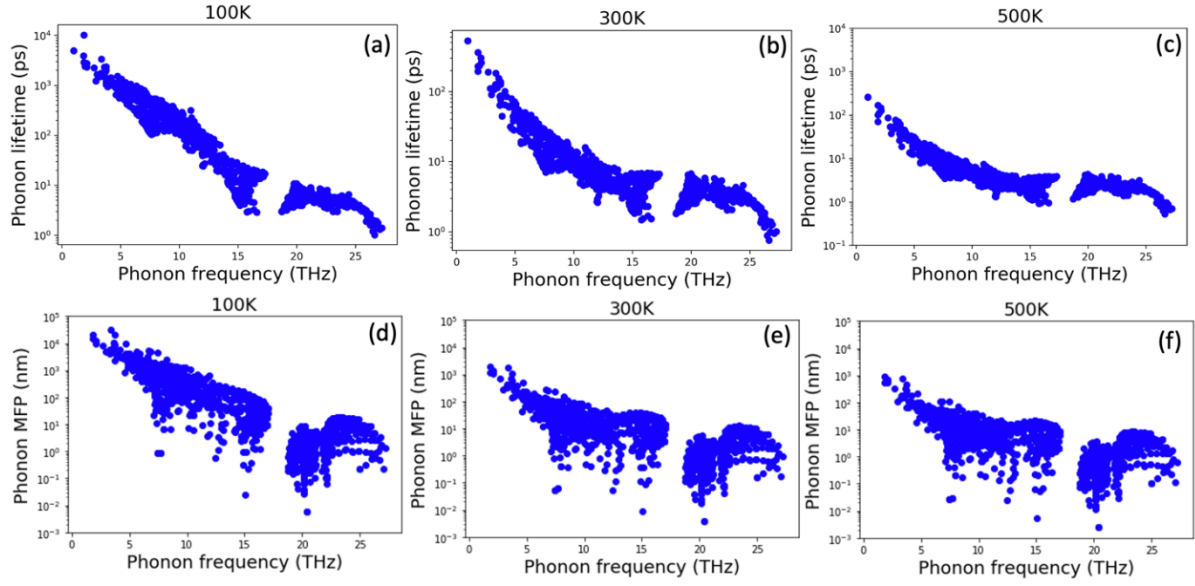


Figure S2 The distribution of phonon lifetime (a)(b)(c) as a function of phonon frequency and the distribution of phonon mean free path (MFP) (d)(e)(f) as a function of phonon frequency calculated from first-principles simulations at selected temperature.

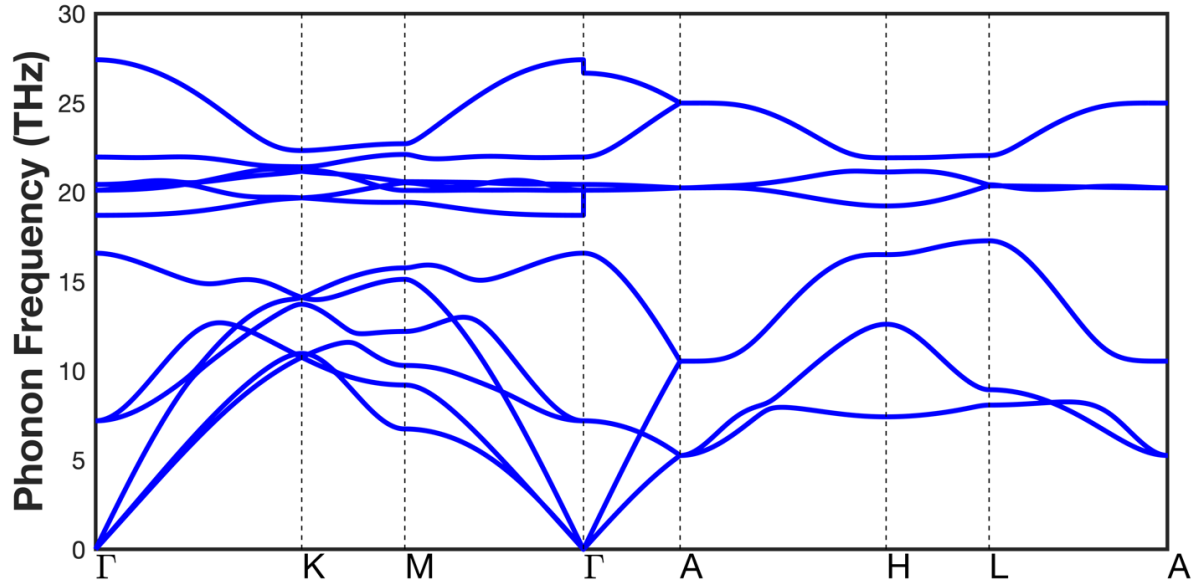


Figure S3 The phonon dispersion of AlN semiconductor along the high symmetry line.

## 2. Thermal penetration depth and the temperature profiles of the 3.05-22 $\mu\text{m}$ AlN films

### A. Time-domain Thermoreflectance Measurements

Most of the previous estimates of the thermal penetration depth in time-domain thermoreflectance (TDTR) measurements are based on the approximation that the thermal penetration depth is  $\sqrt{\kappa/\pi C_p f}$  [S4][S5], which is based on the Gaussian profile with the laser

spot defined as  $\frac{1}{e^2}$ . However, this estimation can be off due to the presence of the Al transducer and interface between transducer/film, especially in the material with high thermal conductivity and low modulation frequency. We applied the model reported in the Ref. [S6], which includes all material properties and sample structures when calculating the precise thermal penetration depth of the TDTR measurements. This model presents temperature profiles for both modulated and unmodulated heating event to reveal the thermal penetration depth based on the  $\frac{1}{e}$  temperature decay of the surface temperature. The difference of the Figure S4 (a) shows the comparison of the thermal penetration depth of the 17.5  $\mu\text{m}$  and 22  $\mu\text{m}$  AlN from the calculated value from Ref. [S6], predicted value from  $\sqrt{\kappa/\pi C_p f}$  estimation (without considering impacts of interfaces) and  $\frac{1}{e^2}$  estimation (with considering impacts of interfaces). The calculated values via Ref. [S6] model is much lower than the predicted values via  $\sqrt{\kappa/\pi C_p f}$  and  $\frac{1}{e^2}$  estimations in the thick AlN samples, 17.5-22  $\mu\text{m}$ . Figure S4 (b)-(e) show the temperature profiles of the 3.05  $\mu\text{m}$  and 22  $\mu\text{m}$  for 1.04 MHz and 8.80 MHz modulation frequencies, respectively. The higher pump modulation frequency measurements are more sensitive to the interface conductance of the Al/AlN. For example, the Al/AlN interface conductance of the 3.05  $\mu\text{m}$  is  $\sim 140 \text{ M W m}^{-2} \text{ K}^{-1}$ , and 17.5  $\mu\text{m}$  is  $\sim 170 \text{ M W m}^{-2} \text{ K}^{-1}$  results in a calculated thermal penetration depth of  $\sim 0.18 \mu\text{m}$  and  $\sim 0.43 \mu\text{m}$ , respectively. However, when the pump modulation frequency becomes lower, the second interface, AlN/Al<sub>2</sub>O<sub>3</sub>, becomes the dominant factor. The AlN/Al<sub>2</sub>O<sub>3</sub> interface does not play any role in 22  $\mu\text{m}$  sample since it is thick enough for the heat to not penetrate to the AlN/Al<sub>2</sub>O<sub>3</sub> interface. Meanwhile, the AlN/Al<sub>2</sub>O<sub>3</sub> interface plays an enormous role in the thinner AlN film, 3.05  $\mu\text{m}$ . This interface confines the heat and increases the total temperature inside the thin films. In other words, the AlN/Al<sub>2</sub>O<sub>3</sub> increases the effective thermal penetration depth in the AlN films. Therefore, the thermal penetration depth in 3.05  $\mu\text{m}$  is  $\sim 3.14 \mu\text{m}$ , larger than  $\sim 1.82 \mu\text{m}$  in 22  $\mu\text{m}$  AlN film. The thermal penetration depth in Figure 4 in the manuscript is calculated based on Ref. [S6] model. The measurement modulation frequency, corresponding thermal penetration depth ( $\frac{1}{e}$  assumption), and the measured thermal conductivity of the AlN films are presented in the Table S2.

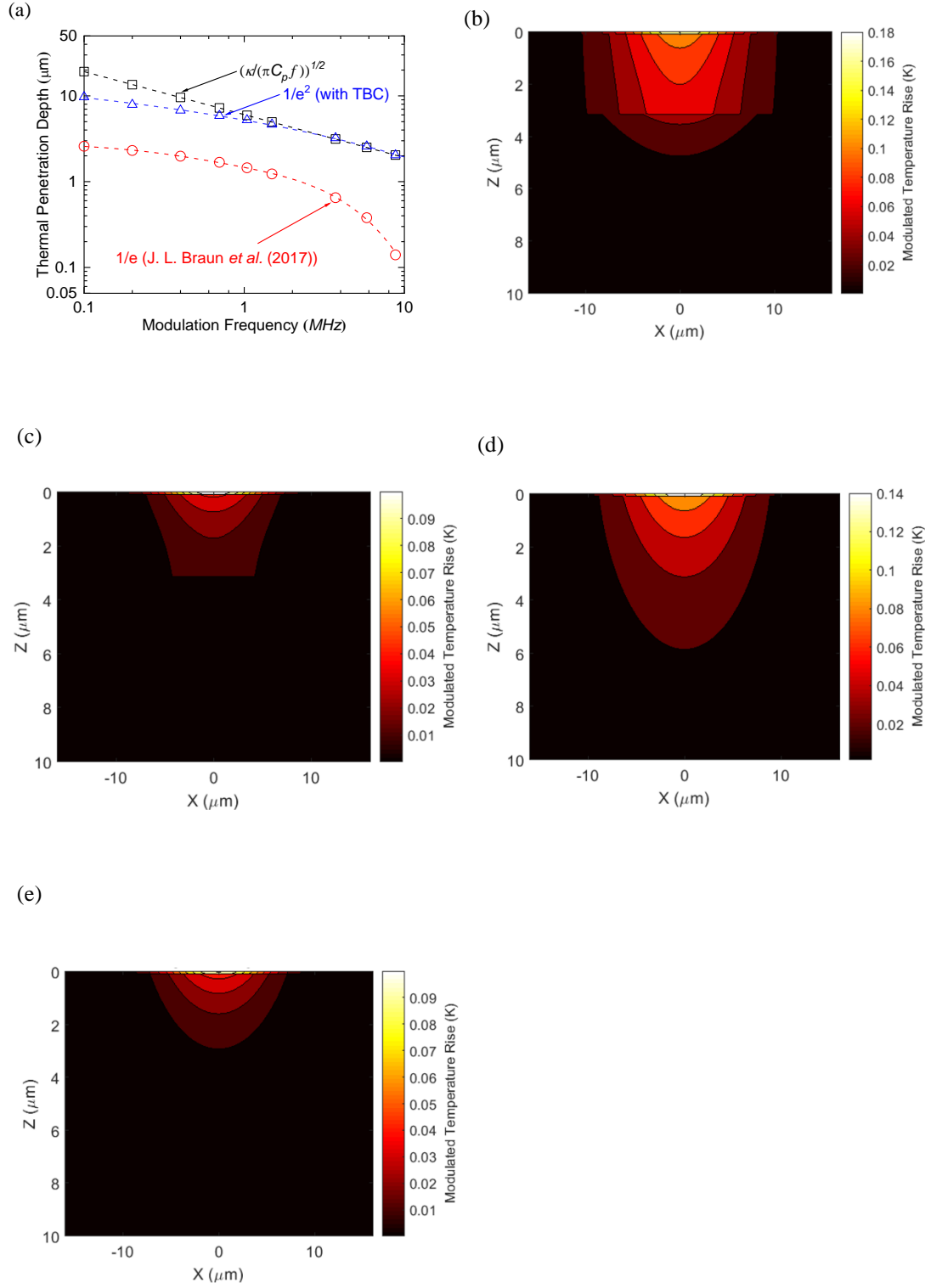


Figure S4 (a) Comparison of the TDTR thermal penetration depth of the 17.5 μm and 22 μm AlN from the calculated value from Ref. [S6], prediction value from  $\sqrt{\kappa/\pi C_p f}$  estimation and  $\frac{1}{e^2}$  estimation with considering TBC effects. Temperature profile of the TDTR measurements are shown in (b) 1.04 MHz, (c) 8.8 MHz of the 3.05 μm, (d) 1.04 MHz, and (e) 8.8 MHz of the 22 μm AlN films.

Table S2 Thermal Penetration Depth and Measured Thermal Conductivity of the AlN Films

$f$ (MHz)	3.05 $\mu\text{m}$ AlN			3.75 $\mu\text{m}$ AlN			6.00 $\mu\text{m}$ AlN			17.50 $\mu\text{m}$ AlN			22.00 $\mu\text{m}$ AlN		
	Thermal Penetration Depth ( $\mu\text{m}$ )	Thermal Conductivity ( $\text{W m}^{-1} \text{K}^{-1}$ )		Thermal Penetration Depth ( $\mu\text{m}$ )	Thermal Conductivity ( $\text{W m}^{-1} \text{K}^{-1}$ )		Thermal Penetration Depth ( $\mu\text{m}$ )	Thermal Conductivity ( $\text{W m}^{-1} \text{K}^{-1}$ )		Thermal Penetration Depth ( $\mu\text{m}$ )	Thermal Conductivity ( $\text{W m}^{-1} \text{K}^{-1}$ )		Thermal Penetration Depth ( $\mu\text{m}$ )	Thermal Conductivity ( $\text{W m}^{-1} \text{K}^{-1}$ )	
1.04	3.14	166.5 $\pm$ 33.5		2.40	177.9 $\pm$ 39.7		1.64	279.7 $\pm$ 44.2		1.82	320.9 $\pm$ 41.8		1.82	319.5 $\pm$ 38.3	
1.49	1.49	324.0 $\pm$ 30.0		1.47	332.0 $\pm$ 47.0		1.34	307.7 $\pm$ 33.8		1.59	326.9 $\pm$ 40.9		1.59	320.0 $\pm$ 38.2	
3.72	0.70	320.0 $\pm$ 42.0		0.59	311.8 $\pm$ 34.3		0.72	324.7 $\pm$ 34.1		0.98	317.8 $\pm$ 40.9		0.98	325.3 $\pm$ 49.3	
5.82	0.32	311.9 $\pm$ 36.9		0.29	309.0 $\pm$ 32.0		0.45	316.4 $\pm$ 44.7		0.68	321.1 $\pm$ 44.2		0.68	318.8 $\pm$ 36.3	
8.80	0.18	321.9 $\pm$ 43.1		0.19	326.6 $\pm$ 48.3		0.22	308.8 $\pm$ 36.3		0.43	313.9 $\pm$ 40.5		0.43	319.8 $\pm$ 41.8	

Penetrate in highly defected region

## B. Steady-state Thermoreflectance Measurements

The SSTR thermal penetration depth in Figure 3(a) of the steady-state thermoreflectance (SSTR) is calculated based on a similar approach in Ref. [S6]. We present a comparison of SSTR thermal penetration depth for  $\frac{1}{e}$  and  $\frac{1}{e^2}$  estimation in Figure S5 (a) below. We used the laser beam size to control the thermal penetration depth in the SSTR measurements. The temperature profiles of the 17.5  $\mu\text{m}$  and 22  $\mu\text{m}$  with laser spot diameters of 11  $\mu\text{m}$  and 20  $\mu\text{m}$  are presented in Figure S5 (b)-(e).

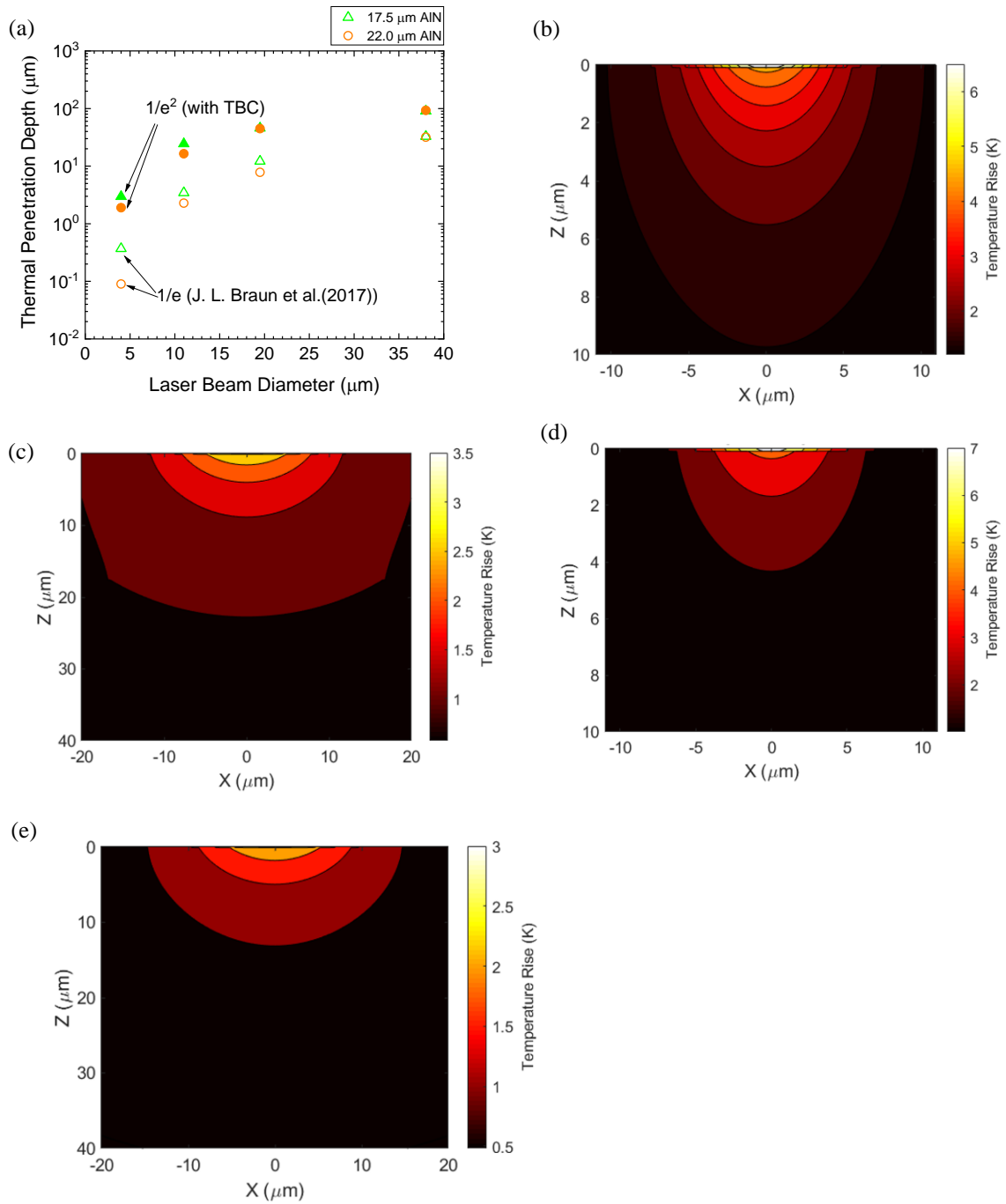


Figure S5 (a) Comparison of the SSTR thermal penetration depth of the 17.5  $\mu\text{m}$  and 22  $\mu\text{m}$  AlN from the calculated value from  $\frac{1}{e}$  and  $\frac{1}{e^2}$  estimation. Temperature profile of the SSTR measurements are shown in (b) 11  $\mu\text{m}$ , and (c) 20  $\mu\text{m}$  laser beam diameter of the 17.5  $\mu\text{m}$ , (d) 11  $\mu\text{m}$ , and (e) 20  $\mu\text{m}$  laser beam diameter of the 22  $\mu\text{m}$  AlN films.

### C. Thermal conductivity versus $\frac{1}{e^2}$ estimated thermal penetration depth

To give a thorough picture of thermal penetration depth, we replicate Figure 3 (a) and Figure 4 from the main manuscript as a function of the  $\frac{1}{e^2}$  estimated thermal penetration depth. This assumes that both SSTR and TDTR measure the AlN films' thermal conductivities at a heater length scale of this thermal penetration depth. The thermal conductivities plotted vs. these  $\frac{1}{e^2}$  thermal penetration depths are presented in Figure S6 (a) and (b). The estimated thermal penetration depth via  $\frac{1}{e^2}$  can be 2-30 times larger than estimated values via  $\frac{1}{e}$ .

The question of the accuracy of the thermal penetration depth estimation can be raised. We believe that  $\frac{1}{e}$  estimated thermal penetration depth might better represent the thermal penetration depth in the AlN measurements in reality, particularly in the TDTR measurements. From the TEM micrographs, we observed a highly defected regime in near AlN/substrate interface with the thickness  $\sim 1.5 \mu\text{m}$ , regardless of the AlN film thickness. We can expect a thermal conductivity reduction once the measurement probes into this regime due to multiple scattering mechanisms, as we had discussed in the main manuscript and in a latter part of this [Supporting Information](#). All of the estimated TDTR thermal penetration depths (all modulation frequency) in thinner AlN films (3.05  $\mu\text{m}$  and 3.75  $\mu\text{m}$ ) via conventional  $\frac{1}{e^2}$  method probes into this highly deflected regime near the Al/substrate interface, shown in Figure S6 (b). No change in the thermal conductivity is measured until the thermal penetration depth of  $\sim 5 - 5.5 \mu\text{m}$ , which is non-physical. We can compare Figure S6 (b) to Figure 4 (or Table S2) in the main manuscript, where we plot the measured thermal conductivity in the function of  $\frac{1}{e}$  estimated thermal penetration depth. The significant reduction in the measured thermal conductivity can be observed once the heat penetrates to the highly deflected regime in 3.05  $\mu\text{m}$  and 3.75  $\mu\text{m}$  AlN films. The measured thermal conductivities remain high and consistent in the high-quality crystalline regime.



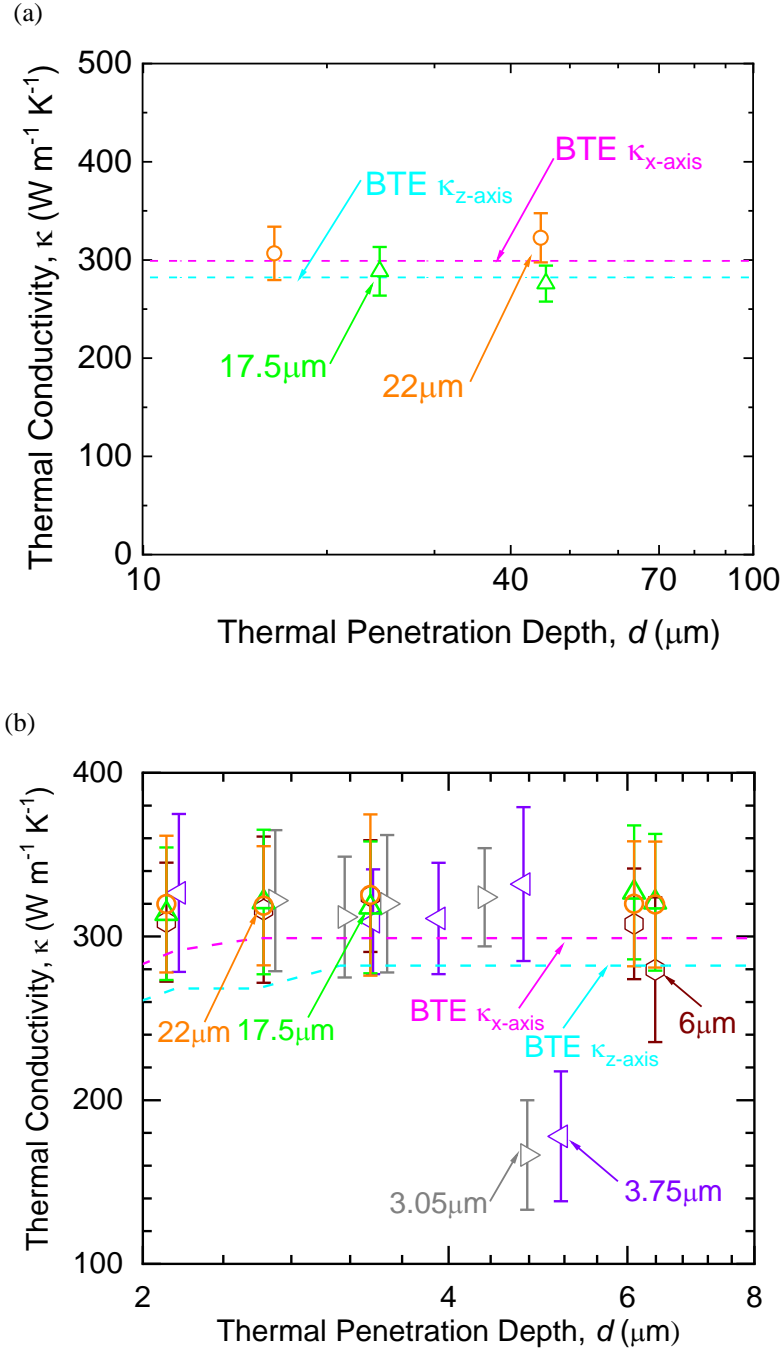


Figure S6 (a) SSTR measurements of the thermal conductivity of AlN films with thicknesses of 17.5  $\mu\text{m}$  (green triangle) and 22.0  $\mu\text{m}$  (orange circle) as a function of  $\frac{1}{e^2}$  estimated thermal penetration depth. Calculated BTE for in- (light blue dashed line) and cross- (pink dashed line) plane thermal conductivity are also included. (b) TDTR measurements of the thermal conductivity of AlN films with various film thicknesses, 3.05–22.0  $\mu\text{m}$ , in-comparison with the calculated BTE thermal conductivity for in- and cross-plane versus  $\frac{1}{e^2}$  estimated thermal penetration depth of the measurements.

### **3. Characterization of the AlN**

#### **A. Raman Spectroscopy Analysis on the AlN Samples**

We employed a Reinshaw Raman InVia Microscopy to analyze the 17.5  $\mu\text{m}$  AlN film, with a 50x objective lens and 488 nm laser. All symmetry-allowed optical phonons in AlN film is dominant by  $E_2$  mode, follows by weaker  $A_1(\text{LO})$ ,  $A_1(\text{TO})$ , and  $E_1(\text{TO})$  modes. Weak Raman spectra for the substrate,  $\text{Al}_2\text{O}_3$  can also be observed in the analysis. All the Raman peaks found in Figure 1(b) in the Ref. [S7] are clean and sharp. This observation verified that the AlN film is high quality, and no intermixing of the impurities and substances present in the film.

#### **B. STEM analysis**

The dislocation density and the microstructures strongly affect the thermal transport of the AlN film. We used the STEM to study and quantify the microstructure and dislocation density of the films. The representative high-resolution STEM micrographs of the 22  $\mu\text{m}$  AlN film are presented in the manuscript (Figure 2 (c-d)). Here, we present another high-resolution plan-view STEM micrograph for on the high-quality single crystal AlN regime (near to the top surface) of the 17.5  $\mu\text{m}$  AlN in Figure S7. We can observe that the film quality in this regime is better compared to the near AlN/ $\text{Al}_2\text{O}_3$  interface regime (shown in Figure 2 (c-d) in manuscript) with lesser defects. The quality is comparable to the near surface regime of 22  $\mu\text{m}$  AlN sample. The dislocation density obtained through this STEM micrograph is also  $\sim 1.6 \times 10^8/\text{cm}^2$ . The dislocation density is found to be one of the lowest among all the industry and laboratory-grade AlN. The details of the relationship between AlN quality and thermal transport, and the comparison of the current best available AlN in the market (Amano and Hexatech) would be further discussed in the Ref. [S7].

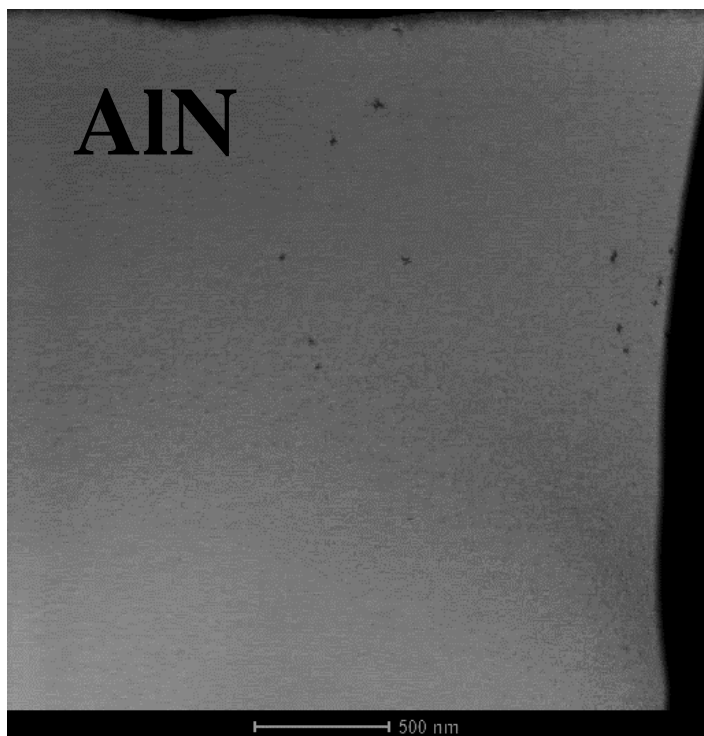


Figure S7 The (11 $\bar{2}$ 0) two beam condition plan-view STEM image shows a few dislocations (appears as dots) near the surface (dislocation density:  $1.6 \times 10^8/\text{cm}^2$ ) for the 17.5 $\mu\text{m}$  AlN film.

We claimed that the nucleation layer thickness near the AlN/Al<sub>2</sub>O<sub>3</sub> interface are almost the same regardless of the total film thicknesses. This claim might not be trivial, especially for the relative thin AlN films, i.e., 3.05  $\mu\text{m}$  and 3.75  $\mu\text{m}$  samples. We performed another STEM analysis on 3.0  $\mu\text{m}$  AlN film. Figure S8 shows the cross-sectional STEM micrographs on the  $\sim 2.5$   $\mu\text{m}$  near AlN/Al<sub>2</sub>O<sub>3</sub> interface of a 3.0  $\mu\text{m}$  AlN film. The STEM analysis shows that the first three micron of the 17.5  $\mu\text{m}$  and 22  $\mu\text{m}$  thick AlN samples are morphologically similar to the 3 $\mu\text{m}$  thick AlN samples in terms of voids and dislocation present. In contrast, the near surface of the thicker samples have lower dislocation densities. This observation is in agreement with TDTR thermal conductivity results. The measured thermal conductivity of the 3.05  $\mu\text{m}$  via 8.8MHz TDTR is ranged in  $\sim 250$ - 330 W m<sup>-1</sup> K<sup>-1</sup> at room temperature depend on the measurement position on the samples, while measured thermal conductivity in 17.5  $\mu\text{m}$  AlN film is consistent  $\sim 320$  W/mK regardless of the measurement position. This result is due to the high-modulation frequency TDTR measurements might likely probing only in the low-quality regimes of the thin AlN film (3.05  $\mu\text{m}$ ), but never probe into these regimes in the thick AlN film (17.5 $\mu\text{m}$ ).

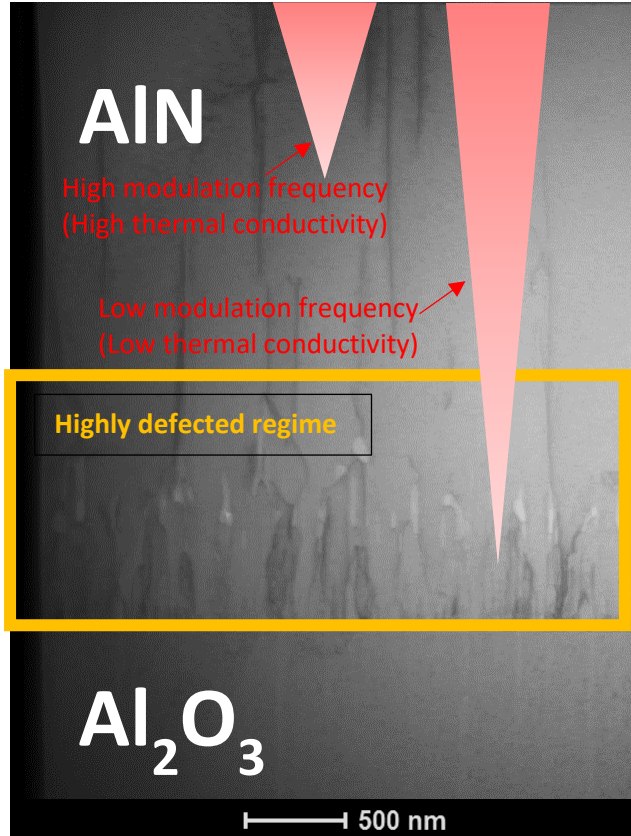


Figure S8 Cross-sectional STEM micrograph on bottom  $\sim 2.5 \mu\text{m}$  near AlN/ $\text{Al}_2\text{O}_3$  interface in a  $3.0 \mu\text{m}$  AlN film.

All the samples regardless of the thickness have similar sample structure, a nucleation layer of AlN formed near the Al/ $\text{Al}_2\text{O}_3$  interface, followed by the low-quality single crystal AlN layer, and a regime of the high-quality single crystal AlN on near the top surface. The thicknesses of the nucleation layer AlN and low-quality AlN layers appear to be  $\sim 0.5\text{-}1.5 \mu\text{m}$  each, regardless of the total film thickness. All the AlN grown above these defected regimes would be the high-quality single crystal AlN.

### C. Secondary Ion Mass Spectrometry (SIMS) Analysis on the AlN Samples

From the previous paragraphs, we knew that the AlN film quality is essential for the studies of the thermal transport of thin films. Besides the dislocations and microstructure, the quality of the films also can be related to the impurities contains. The impurities, i.e., Si, C, and O, can be analyzed by using SIMS technique shown here.

Slack [S8] showed that the oxygen vacancy had a considerable impact to the thermal conductivity on the AlN bulk. Ref. [S1] also performed the theoretical analysis to calculate the impacts of the impurity density on the AlN thermal conductivity. Slack's measured thermal conductivity of the AlN bulk is  $\sim 280 \text{ W m}^{-1} \text{ K}^{-1}$ , with the extrapolation of the "perfect" AlN thermal conductivity would be  $\sim 320 \text{ W m}^{-1} \text{ K}^{-1}$ . Some other *ab-initio* analysis [S9] shows the consistent results with the Slack's extrapolation of the "perfect" AlN bulk in the room temperature. However, the calculated bulk AlN thermal conductivity via the first-principle calculations has never been measured. Even with the improvement of the material growth techniques, most of the literature still report the measured thermal conductivity of the AlN films and bulks is  $\sim 280 \text{ W m}^{-1} \text{ K}^{-1}$  in the past few decades.

We believe that the impurities contain in the AlN might be the "key" for achieving theoretical AlN bulk thermal conductivity at room temperature. Here, we show the SIMS analysis of the  $17.5\mu\text{m}$  MOCVD grown AlN film used in the paper. The analysis comparison in SIMS is made on the MOCVD grown AlN, high-quality Hexatech, and Amano grown AlN bulk, which are the best available industry-grade AlN films. Figure S9 (a-c) shows the SIMS results on the C, O and Si impurities respectively of the MOCVD, Amano, and Hexatech grown AlN samples. The SIMS results show that the MOCVD grown AlN film at least 50 times lower in C, O and Si impurities than the AlN samples from Amano and Hexatech.

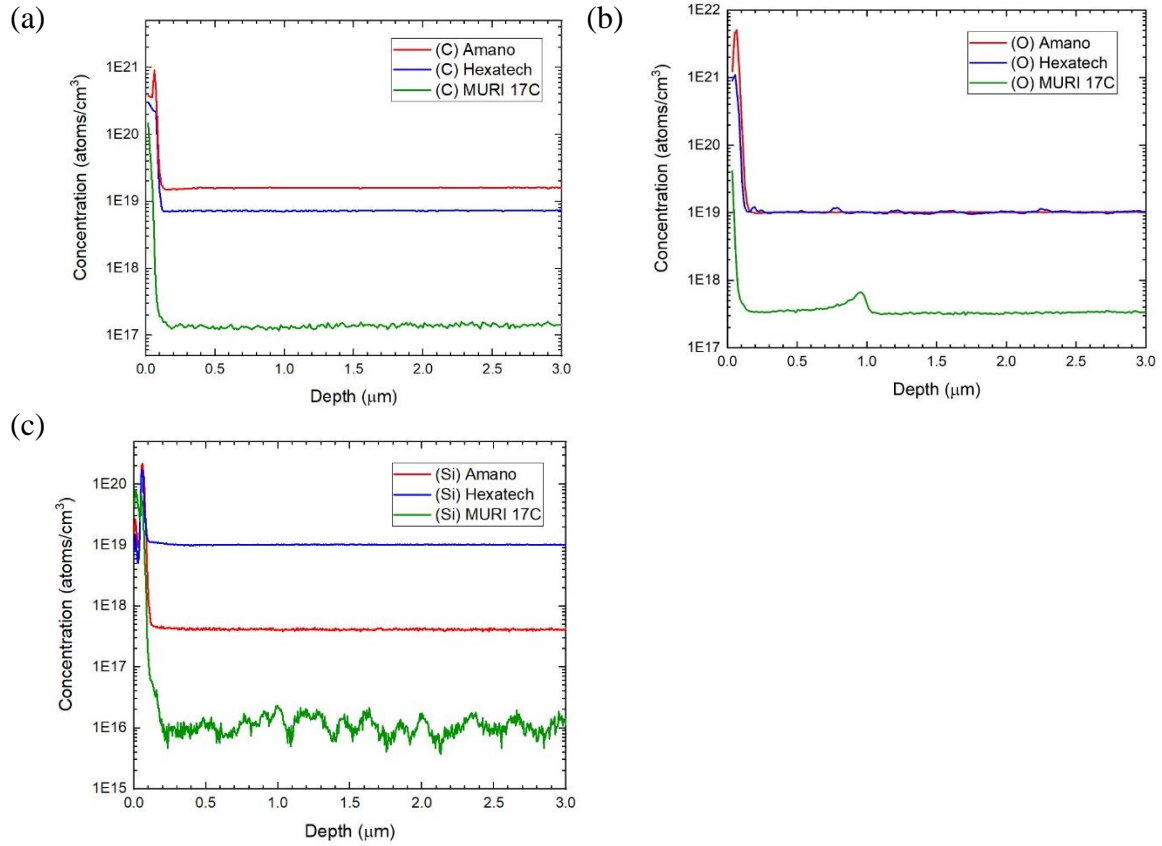


Figure S9 SIMS analysis of the a) C, b) O, and c) Si impurities on the 17.5μm AlN, Amano, and Hexatech AlN samples.

#### 4. Steady-state Thermoreflectance (SSTR) Sensitivity Analysis

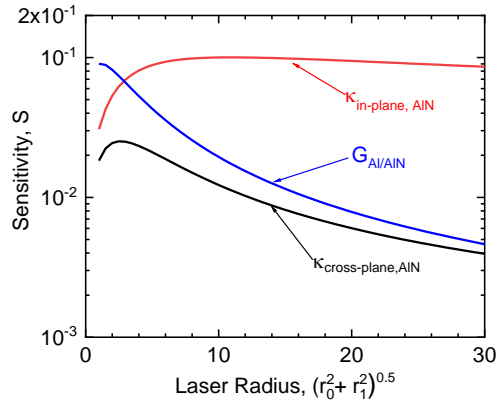
We employed a new technique, steady-state thermoreflectance (SSTR) [S10] to measure the AlN samples. However, the measured thermal conductivity for the samples is not necessary to represent what we expect. In the manuscript, we only present the SSTR measurement results of the 17.5 μm and 22 μm AlN films. We do not present SSTR measurement results on the thinner AlN samples, i.e., 3.05 μm, 3.75 μm, and 6 μm AlN films. In the high thermal conductivity thin films measurements, SSTR measurement is sensitive in the in-plane thermal conductivity but not sensitive in measuring the cross-plane thermal conductivity. We required a thick enough sample so that the effective cross-plane thermal conductivity can be measured. The in-plane and cross-plane thermal conductivity sensitivity in SSTR are similar if the spot size is  $r < 3 \mu\text{m}$  in 17.5 μm and 22 μm AlN film, while the cross-plane thermal conductivity sensitivity drops to barely half of the in-plane thermal conductivity when laser spot size increase. On the thinner films, 3.05 μm, 3.75 μm, and 6 μm side, the in-plane thermal conductivity sensitivity is always ~5-10 times higher than the cross-plane thermal conductivity,

regardless of the spot size. We can conclude that SSTR measurements are not sensitive to the cross-plan thermal conductivity of the 3.05 $\mu\text{m}$ , 3.75 $\mu\text{m}$ , and 6 $\mu\text{m}$  AlN samples. Figure S10 (a-e) show the sensitivity versus laser spot radius of the 3.05 $\mu\text{m}$ , 3.75  $\mu\text{m}$ , 6  $\mu\text{m}$ , 17.5  $\mu\text{m}$  and 22  $\mu\text{m}$  AlN films respectively.

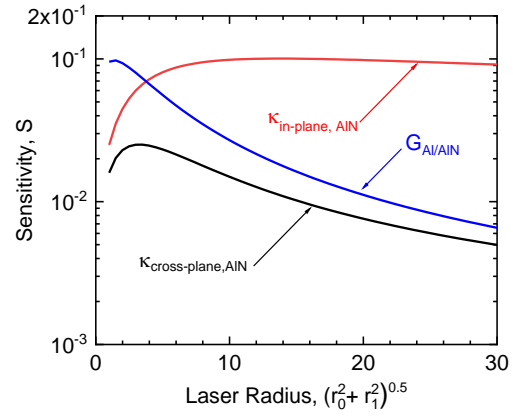
The thermal conductivity of the AlN is assumed as 300 W m<sup>-1</sup> K<sup>-1</sup> in 3.05  $\mu\text{m}$ , 3.75  $\mu\text{m}$ , 6  $\mu\text{m}$ , 17.5  $\mu\text{m}$ , and 22  $\mu\text{m}$  in the sensitivity analysis. Other parameters, i.e. specific heat capacity, AlN/Al<sub>2</sub>O<sub>3</sub> interface conductance etc. are consistent in all analysis. Sensitivity of the SSTR is different to the TDTR [S11], is defined as  $S_x = \frac{|\Delta T_{1.1x}(r_{01}) - \Delta T_{0.9x}(r_{01})|}{\Delta T_x(r_{01})}$ , where  $\Delta T_x$  is the temperature rise calculated for the input parameter  $x$  and  $r_{01} = \sqrt{r_{probe}^2 + r_{pump}^2}$ . [S4]

By using the objective lens with different magnification, we can control different radii of laser spot size from ~2-20  $\mu\text{m}$ . From the SEM and STEM analysis, we know that the high-quality monocrystalline AlN only appears on the top few microns depend on the total thickness of the sample. We expect that measured thermal conductivity via SSTR is equal with the TDTR measurement in thick AlN samples (17.5  $\mu\text{m}$  and 22  $\mu\text{m}$ ). The measured thermal conductivity of these thick AlN sample is shown in Figure 4. The measured SSTR thermal conductivity of the 17.5  $\mu\text{m}$  and 22  $\mu\text{m}$  are in line with the expectation, with a consistent value  $300 \pm 30 \text{ W m}^{-1} \text{ K}^{-1}$  in 2-20  $\mu\text{m}$  penetration depth. The measured thermal conductivity of 3.0-6.0  $\mu\text{m}$  via SSTR are not presented in the Figure 3 (a) of the manuscript. SSTR measurements are insensitive to the cross-plane thermal conductivity in 3.0-6.0  $\mu\text{m}$  AlN films. In general, the measured SSTR thermal conductivity is approximately a  $\sqrt{k_r k_z}$ , identical sensitive to both cross-plane and in-plane in bulk and thick films, with  $k_r$  is in-plane thermal conductivity and  $k_z$  is cross-plane thermal conductivity. Sensitivity of the SSTR thermal conductivity measurements is reduced to an approximately a  $\sqrt{k_r^2}$ , relation in thin AlN films due to the continuous wave behavior. The measured in-plane thermal conductivity  $k_r$  is a convoluted result from the all regimes, i.e., high-quality single crystal, defects-rich single crystal and nucleation regime, which is hard to be interpreted. We had only included the cross-plane thermal conductivity here, while the in-plane thermal transport would be interesting for the future study.

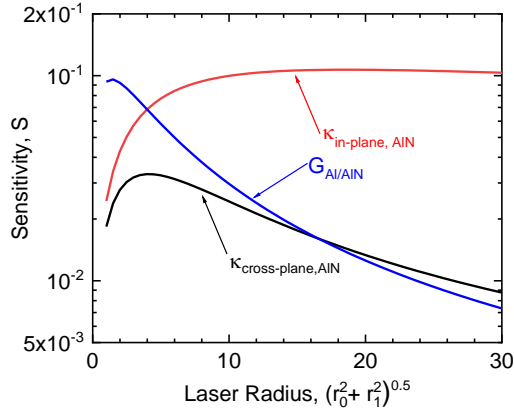
(a)



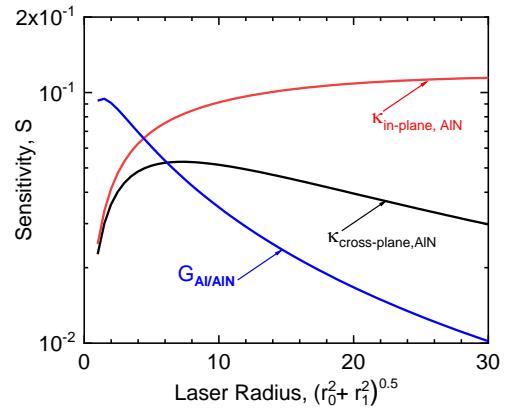
(b)



(c)



(d)



(e)

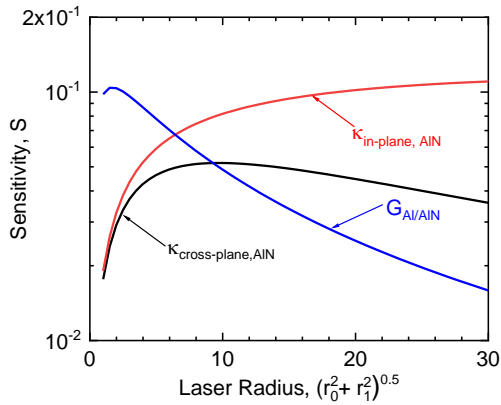


Figure S10 Sensitivity of the (a) 3.05  $\mu\text{m}$ , (b) 3.75  $\mu\text{m}$ , (c) 6  $\mu\text{m}$ , (d) 17.5  $\mu\text{m}$  and (e) 22  $\mu\text{m}$  versus laser spot size  $\sqrt{r_0^2 + r_1^2}$ , where  $r_0$  is probe radius and  $r_1$  is pump radius.



## 5. Calibration of the TDTR System

There are limited available thermal conductivity techniques/options that provide reliable measurements on films with thicknesses in the range of submicrons to microns. The optical pump-probe TDTR method is proven as an effective experimental technique in studies of the thermal conductivity of thin films and thermal boundary conductance of interface in the past few decades. Prior to the optical pump-probe technique, the  $3\omega$  method [S12] provided a trusted measurements technique for thin film thermal conductivity characterization. Koh *et al.* (2009) [S13] had made a comparison of  $3\omega$  method and time-domain thermoreflectance for the measurements of the cross-plane thermal conductivity of epitaxially grown semiconductor films  $((\text{In}_{0.52}\text{Al}_{0.48})_x(\text{In}_{0.53}\text{Ga}_{0.47})_{1-x}\text{As})$ . Their results show that the measured thermal conductivities of this thin film alloy can agree within experimental uncertainties. These results prove that TDTR is reliable and can be accepted as a reference method to measure the thermal conductivity of thin films. We note that several recent review articles have also highlighted TDTR as the current state of the art for thermal conductivity measurements of thin films.[S14][S15]

In our current manuscript, we have calibrated our TDTR setup with sapphire, prior to the AlN thin film measurements versus temperature. Figure S11 below shows a comparison of the measured sapphire thermal conductivity as a function of temperature via TDTR and  $3\omega$  method [S16]. The measured sapphire thermal conductivity via a separate TDTR system at Georgia Tech [S17] is also included in the comparison. The obtained sapphire thermal conductivity though these TDTR systems (UVa and Georgia Tech) matches well to the measured value measured from the  $3\omega$  method. The calibration results on the sapphire thermal conductivity as a function of temperature verify the accuracy of the measured thin film thermal conductivity.

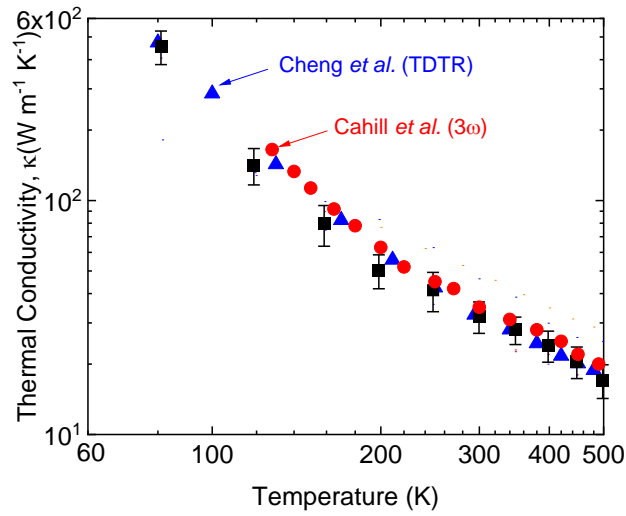


Figure S11 Thermal conductivity of sapphire in the function of 3 $\omega$  method [S12] and TDTR systems [S13].

Our TDTR measurements are sensitive to the total thermal resistance in the through-plane direction of the samples, which includes the resistance from the metal transducer, interfaces, substrate, etc. We agree that it is challenging to measure high thermal conductivity thin-film materials accurately due to the relatively small thermal resistance of this cross-plane thermal transport property. The direct comparison of the measured thermal conductivity of 22  $\mu\text{m}$  AlN and current best commercial AlN bulk from Hexatech via the same TDTR system, is shown in Figure S12. These results/comparisons had been reported in our previous work in Ref. [S7]. The measured thermal conductivity of the 22  $\mu\text{m}$  AlN is comparable to Hexatech AlN bulk in the 300-500K regime, and significantly higher in the 120-300K regime, under the same TDTR system and fitting assumption/model. Overall, this observation confirms ultrahigh crystalline quality in the AlN film and results in higher thermal conductivity. We had also included the measured thermal conductivity of the AlN bulk with the 3 $\omega$  method [S1], which is comparable to the TDTR measured results.

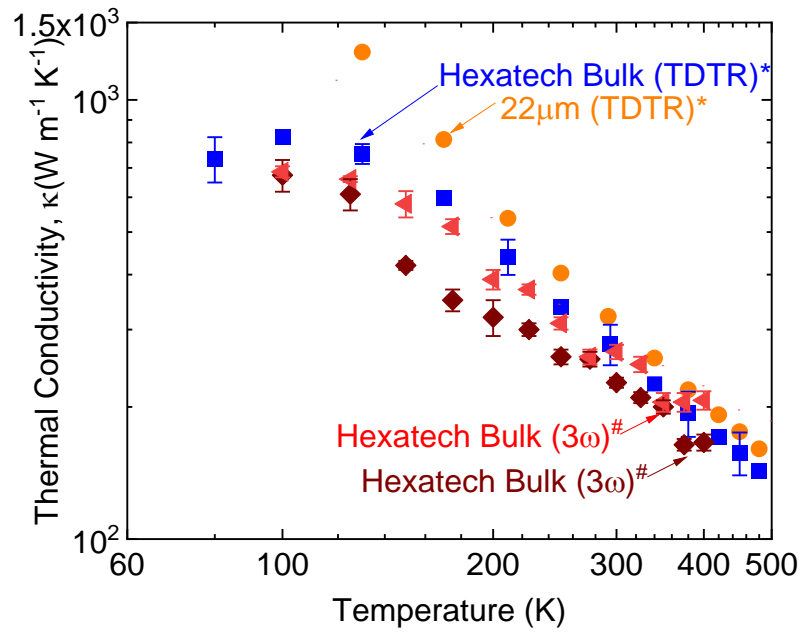


Figure S12 Measured thermal conductivity of 22 AlN film via TDTR [S7], and Hexatect AlN bulk via TDTR [S7] and 3 $\omega$  method [S1].

## References

- [S1] Xu, R.; Rojo, M. M.; Islam, S. M.; Sood, A.; Vareskic, B.; Katre, A.; Mingo, N.; Goodson, K. E.; Xing, H. G.; Jena, D.; Pop, E. Thermal conductivity of crystalline AlN and the influence of atomic-scale defects. *J. Appl. Phys.* **2019**, 126, 185105.
- [S2] Aissa, K. A.; Semmar, N.; Meneses, D. D. S.; Brizoual, L. L.; Gaillard, M.; Petit, A.; Jouan, P.-Y.; Boulmer-Leborgne, C.; Djouadi, M. A. Thermal conductivity measurement of AlN films by fast photothermal method. *Journal of Physics: Conference Series* **2012**, 395, 012089.
- [S3] Freedman, J. P.; Leach, J. H.; Preble, E. A.; Sitar, Z.; Davis, R. F.; Malen, J. A. Universal Phonon Mean Free Path Spectra in Crystalline Semiconductors at High Temperature. *Sci. Rep.* **2013**, 3, 2963.
- [S4] Koh, Y. K.; Cahill, D. G. Frequency Dependence of the Thermal Conductivity of Semiconductor Alloys. *Phys. Rev. B* **2007**, 76, 075207.
- [S5] Regner, K. T.; Sellan, D. P.; Su, Z.; Amon, C. H.; McGaughey, A. J. H.; Malen, J. A. Broadband Phonon Mean Free Path Contributions to Thermal Conductivity Measured using Frequency Domain Thermoreflectance. *Nat. Commun.* **2013**, 4, 1640.
- [S6] J. L. Braun and P. E. Hopkins, Upper limit to the thermal penetration depth during modulated heating of multilayer thin films with pulsed and continuous wave lasers: A numerical study. *J. Appl. Phys.* **2017**, 121, 175107.
- [S7] Cheng, Z.; Koh, Y. R.; Mamun, A.; Shi, J.; Bai, T.; Huynh, K.; Yates, L.; Liu, Z.; Li, R.; Lee, E.; Liao, M. E.; Wang, Y.; Yu, H. M.; Kushimoto, M.; Luo, T.; Goorsky, M. S.; Hopkins, P. E.; Amano, H.; Khan, A.; Graham, S. Experimental Observation of High Intrinsic Thermal Conductivity of AlN. *Phys. Rev. Mater.* **2020**, 4(4), 044602.
- [S8] Slack, G. A.; Tanzilli, R. A.; Pohl, R. O.; Vandersande, J. W. The Intrinsic Thermal Conductivity of AlN. *J. Phys. Chem. Solids* **1987**, 48(7), 641-647.
- [S9] Lindsay, L.; Broido, D. A.; Reinecke, T. L. Ab Initio Thermal Transport in Compound Semiconductors. *Phys. Rev. B* **2013**, 87, 165201.
- [S10] Braun, J. L.; Olson, D. H.; Gaskins, J. T.; Hopkins, P. E. A Steady-state Thermoreflectance Method to Measure Thermal Conductivity. *Rev. Sci. Instrum.* **2019**, 90, 024905.
- [S11] Jiang, P.; Qian, X.; Yang, R. Time-domain Thermoreflectance (TDTR) Measurements of Anisotropic Thermal Conductivity Using A Variable Spot Size Approach. *Rev. Sci. Instrum.* **2017**, 88, 074901.
- [S12] Cahill, D. G.; Pohl, R. O. Thermal conductivity of amorphous solids above the plateau. *Phys. Rev. B.* **1987**, 35, 4067–4073.
- [S13] Koh, Y. K.; Singer, S. L.; Kim, W.; Zide, J. M. O.; Lu, H.; Cahill, D. G.; Majumdar, A.; Gossard, A. C. Comparison of the  $3\omega$  method and time-domain thermoreflectance for measurements of the cross-plane thermal conductivity of epitaxial semiconductors. *J. Appl. Phys.* **2009**, 105, 054303.
- [S14] Cahill, D. G.; Ford, W. K.; Goodson, K. E.; Mahan, G. D.; Majumdar, A.; Maris, H. J.; Merlin, R.; Phillpot, S. R. Nanoscale thermal transport. *J. Appl. Phys.* **2003**, 93(2), 793-818.

- 
- [S15] Cahill, D. G.; Braun, P. V.; Chen, G.; Clarke, D. R.; Fan, S.; Goodson, K. E.; Keblinski, P.; King, W. P.; Mahan, G. D.; Majumdar, A.; Maris, H. J.; Phillpot, S. R.; Pop, E.; Shi, Li. Nanoscale thermal transport. Ii. 2003-2012. *Appl. Phys. Rev.* **2014**, 1(1), 011305.
- [S16] Cahill, D. G.; Lee, S. M.; Selinder, T. I. Thermal conductivity of  $\kappa$ -Al<sub>2</sub>O<sub>3</sub> and  $\alpha$ -Al<sub>2</sub>O<sub>3</sub> wear-resistant coatings. *J. Appl. Phys.* **1998**, 83, 5783-5786.
- [S17] Cheng, Z., Koh, Y.R., Ahmad, H., Hu, R., Shi, J., Liao, M.E., Wang, Y., Bai, T., Li, R., Lee, E., Yates, L., Luo, T., Goorsky, M., Doolittle, W., Tian, Z., Hopkins, P., Graham, S., Thermal Conductance Across Harmonic-matched Epitaxial Al-sapphire Heterointerfaces. **2019**, arXiv:1906.05484.